JOURNAL OF AIRCRAFT
Vol. 48, No. 2, March–April 2011

High-Lift Multi-Element Airfoil Shape and Setting Optimization Using Multi-Objective Evolutionary Algorithms

Ernesto Benini,* Rita Ponza,† and Andrea Massaro‡
University of Padova, 35131 Padova, Italy

DOI: 10.2514/1.C031233

A multi-objective and multipoint optimization problem is presented dealing with a multi-element airfoil used in high-lift devices (including slat, main, and flap components). The purpose is to enhance its aerodynamic performance at both takeoff and landing operations by searching for optimal shape and setting parameters for both slap and flap. The procedure is driven by a multi-objective genetic algorithm coupled with an Euler/boundary-layer flow solver that speeds up the objective function evaluations, while a Navier–Stokes computational fluid dynamics solver is used for final solutions verification. The final Pareto Optimal solutions are presented and the reasons for improved performance are discussed.

Nomenclature

C_D	=	airfoil drag coefficient
C_L	=	airfoil lift coefficient
$C_{m1/4}$	=	airfoil moment coefficient at $0.25c$
C_p	=	pressure coefficient
c	=	airfoil chord
$F_{\mathrm{TO}} = F_1$	=	objective function for takeoff
$F_{\mathrm{LDG}} = F_2$	=	objective function for landing
$\mathbf{F}$	=	two-objective function
P_L	=	penalty function
R^2	=	correlation coefficient
Re	=	Reynolds number
x/c	=	nondimensional chordwise coordinate
x_{dep}, y_{dep}	=	nondimensional coordinates of deployed component
y^+	=	nondimensional wall distance
α	=	angle of attack
β	=	penalty coefficient
δ	=	setting rotation
δ^*	=	nondimensional boundary-layer displacement thickness
θ	=	nondimensional boundary-layer momentum thickness

Introduction

A PROPER design of multi-element high-lift systems has gained increasing importance, due to the huge impact it may have on the overall sizing, costs, and safety issues of the majority of transport aircraft configurations [1,2].

While in the past the design objectives were mainly targeted to maximum lift requirements [2], in recent years more attention has been given to the reduction of both complexity and weight of high-lift devices for assigned maximum lift values, which gives a beneficial effect on the overall cost of the aircraft. In fact, it is not uncommon for an aircraft high-lift system to account for about 10% of the production cost of a typical jet transport [3]. In fact, such systems typically require a lot of time to be designed and tested; moreover, their actuation and support systems are quite complex to be developed; finally, they are usually heavy and need intensive maintenance. Nevertheless, they are necessary for achieving reasonable runway lengths in takeoff (T-O) and landing (LDG) of transport airplanes while preserving cruise efficiency.

To this purpose, it has been evidenced [4] that even small improvements of high-lift systems aerodynamic characteristics can produce significant gains in the aircraft overall weight and performance. Actually, a leading-edge (LE) device such as a slat increases the wing stall angle, while a trailing-edge (TE) device such as a flap acts in the direction of shifting upwards the wing lift curve. It has been observed that the aerodynamic performance of multi-element wings is very sensitive to the settings of the various elements (gap and overlap extent, angle of rotation); moreover, the system needs to feature good efficiency for multiple flight conditions (light and heavy T-O, LDG) in which large aerodynamic loads typically arise over the various elements. This is the reason why increasing efforts have been addressed toward both the analysis and optimization of such kind of devices.

The complexity of the flowfield developing around multi-element high-lift configurations has led until the recent past to a substantially empirical approach for their analysis and design. However, the most recent advances in computational methods for aerodynamic design have allowed for intensive and time consuming experimental trials to be progressively substituted by numerical analyses such that examples of computational fluid dynamics (CFD) computations on multi-element airfoil are nowadays almost uncountable [2]. Anyway, the design of high-lift systems using numerical computation techniques is still a challenging task, primarily due to many complex features usually difficult to be captured by CFD, such as multiple laminar to turbulent transitions [5], wakes interactions with boundary layers, and regions of flow detachment [6].

Several examples of CFD computations of high-lift systems are found in open literature. A good and relatively recent review is given in [7]. Flows over multi-element airfoils have been traditionally analyzed using interaction methods which employ separate inviscid and viscous flow solvers coupled in an interactive manner [8–11]. More recently, 2-D Reynolds-averaged Navier–Stoke (RANS) methods have also been successfully applied (see [2] for a review).

Also, aerodynamic optimization studies, including multi-objective methodologies, have been successfully performed. Among others, in [12] a single-point method for optimizing the geometry and position of high-lift system elements based on an incompressible flow solver was presented which maximized lift for a given drag at takeoff and LDG configurations.

A two-dimensional aircraft high-lift system design and optimization method based on a gradient-based local optimizer was presented in [13], where the aerodynamic performance was predicted using an interactive boundary-layer (IBL) approach and flap shape functions as well as element positioning (deflection angle, gap,

Received 8 September 2010; revision received 10 December 2010; accepted for publication 11 December 2010.

*Research Professor, Department of Mechanical Engineering, Via Venezia. Member AIAA.
†Postgraduate researcher.
‡Postgraduate researcher.

overlap) were considered. The objective considered was the lift-to-drag ratio and single airfoil maximum lift coefficient maximization.

A numerical optimization procedure using the adjoint method for high-lift system design has been developed and presented in [14], where shape and deflection angles of the slat and flap elements are used for C_D minimization and C_L maximization subject to several kinds of constraints. Moreover, in [15] a Newton–Krylov (gradient-based) algorithm was presented for the aerodynamic optimization of a multi-element airfoil, where the objective function sensitivities were calculated using an adjoint formulation with the purpose of lift-enhancement and multipoint lift-constrained drag minimization.

More recently, in [16] an aerodynamic design of high-lift multi-element airfoil is conducted based on a gradient-based optimization method using a 2-D Navier–Stokes solver and sensitivity analysis method. In [17], a single-objective optimization procedure has been developed and applied to the design optimization of both flap and slat settings (their shape being fixed) in a three-element airfoil. The authors described the use of an interactive flow solver coupled with a genetic algorithm to minimize drag at 10° angle of attack and, separately, maximize lift-to-drag ratio for the same incidence angle. In [18], several optimization cases are presented (lift maximization at landing, lift-to-drag maximization at takeoff) to accomplish flap and slat shape design optimizations including uncertain operating conditions; these cases were handled with using single-objective evolutionary algorithms and a response surface methodology. A very recent work was also published [19] where a systematic CFD optimization study was carried out with a genetic algorithm based design optimization procedure on a foil in water.

Other known examples of design optimization studies can be found in the open literature [20].

Also, multi-objective approaches, especially those based on multi-objective evolutionary algorithms (MOEAs) have been used to tackle this problem in view of their superior ability, compared with more conventional gradient-based techniques, to handle multi-objective problems where highly nonlinear and multimodal functions are to be dealt with. For instance, a multi-objective constrained optimization of multi-element airfoils is presented in [21] aiming at maximizing lift force on multi-element through the search for optimal flap setting using a MOGA. A study was also given in [22], where different optimization strategies (including MOEAs), as well as different types of flow solvers were used with the aim of improving lift and drag performance of a multi-element airfoil at takeoff by redesigning its TE flap.

In the present paper, a step beyond the above mentioned applications, particularly the one presented in [22], is given. Here a multicomponent airfoil design procedure, aimed at enhancing its aerodynamic performance, is presented and applied to a challenging multisetting, multipoint design case, where the shape and setting of both slat and flap are optimized for both T-O and LDG conditions. The procedure is driven by a multi-objective genetic algorithm coupled with an Euler/boundary-layer flow solver, which speeds up the objective function evaluations, while for final solutions' verification a Navier–Stokes CFD solver is used.

First, the peculiar features of the design case are presented and discussed; then the flow solver used for objective function evaluation is validated against experimental data. Finally, the optimization methodology is described in detail and the obtained optimal solutions are presented and verified.

Description of the Design Test Case

The selected baseline geometry for optimization task is the case A-2 from AGARD-AR 303 [22], which is a two-dimensional supercritical airfoil, referred to as NHLP 2-D (configuration L1T2), with high-lift devices consisting of a 12.5%c leading-edge slat and a 33%c single slotted flap, being $c = 0.7635$ m the chord length of the retracted airfoil (Fig. 1). The slat and flap are deflected 25 and 20°, respectively, which is a configuration typical of a T-O condition.

Wind-tunnel tests were carried out at a freestream Mach number $M = 0.197$ and at a Reynolds number $Re = 3.52 \cdot 10^6$, based on the stowed geometry chord; moreover, transition was tripped on the main element at $x/c = 0.125$ on both the upper and lower surface, while it was left free over the slat and flap.

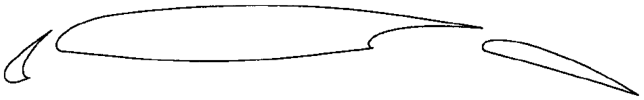

Fig. 1 NHLP 2-D L1T2 high-lift airfoil design test case, from [22].

Data gathered consisted of surface pressure distributions over the model at different angles of attack, static and total pressure variations through both the wake and boundary layers at different chordwise locations and integrated lift, drag, and moment coefficients for a wide extension of incidences.

Flow Solvers: Description and Validation

Aerodynamic performance of an airfoil equipped with high-lift devices is governed by both inviscid and viscous effects. It follows that for the optimization of a multi-element airfoil a computational method capable of capturing viscous as well as inviscid flow phenomena must be used for objective function evaluation.

However, while Navier–Stokes CFD tools (often referred to as "high-fidelity" solvers) are nowadays routinely used in the analysis of high-lift configurations, they are usually quite computationally demanding. More suitable tools for objective function evaluation are the so-called "interaction methods" or "lower-fidelity" solvers, which employ separate inviscid and viscous flow solvers coupled in an interactive way; actually, these methods are far less computationally expensive than the Navier–Stokes solvers, thus allowing to accelerate convergence toward a good estimation of the global optima. Despite being considered less accurate with respect to CFD solvers, they can be profitably used within an optimization procedure involving multi-element airfoils provided that a rigorous validation is previously carried out.

In this work, two flow solvers were selected according to the criteria described above. The first code is the viscous/inviscid interaction code MSES by Drela ([23,24]). The second is the well-known, commercial CFD Fluent™ code [25].

In MSES, a streamwise-based discretization of the Euler equations is used to compute the inviscid flowfield. Then, an integral formulation including a transition prediction methodology is applied for characterization of boundary layers. Finally, the viscous and inviscid solutions are coupled through both the displacement thickness and edge velocity, using a Newton method to solve the coupled system of equations. This strong coupling between the inviscid and viscous solutions allows capturing moderate flow separation typically occurring over multi-element airfoils nearby the slat and the main element cove where, in spite of the large recirculation, numerical results are much easier to be obtained due to the evident geometrical separation point. It is worth noting that the code has the intrinsic capability to adapt grid during the simulation, according to the actual flowfield being calculated. As a consequence, even though large separation regions cannot be captured properly, the code is able to identify them while skipping the meshing where the flow is largely separated.

Fluent™ solves for the compressible RANS equations using a finite volume method on both unstructured and structured grids, while a collection of turbulence models are used to account for flow-wall interaction and viscosity-related phenomena.

In the present paper, MSES was used as the primary objective functions' evaluator within the optimization loop, while Fluent™ was used to check the optimal solutions obtained after the optimization. This is a common practice in aerodynamic optimization [17], where the high-fidelity solver is used to validate solutions obtained using a lower-fidelity tool. However, both the solvers underwent a validation process to assess their reliability, as described later on.

The reliability of both MSES and Fluent™ codes in predicting the aerodynamic performance of multi-element airfoils has been assessed against experimental data over the NHLP 2-D L1T2 airfoil

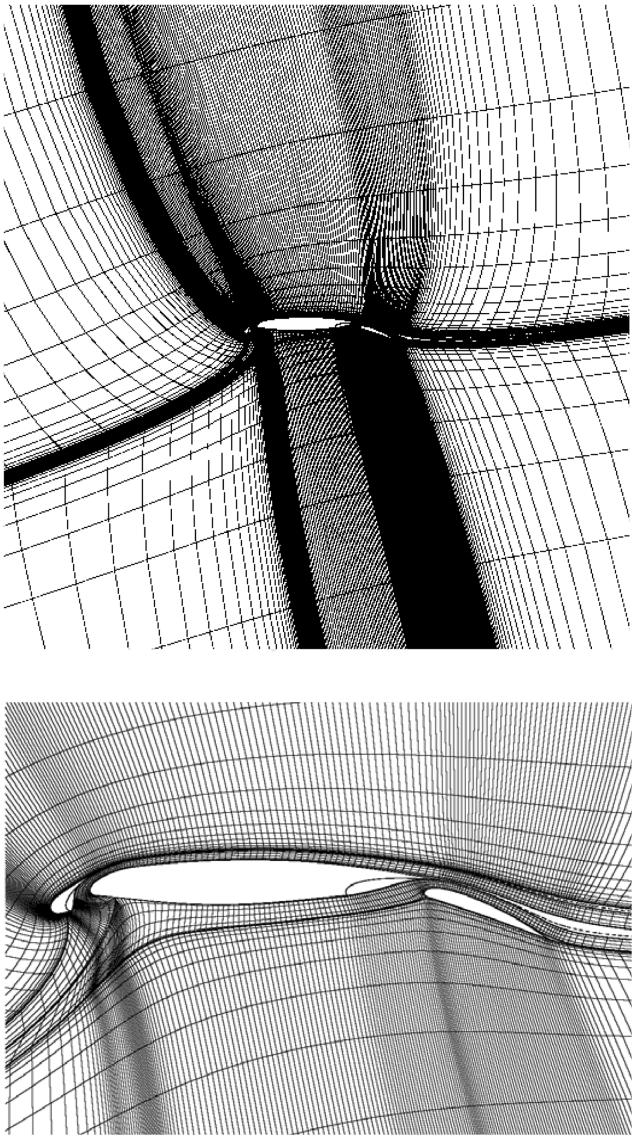

Fig. 2 Global view (upper) and close-up (lower) of the grid used for MSES code validation on the NHLP 2-D L1T2 airfoil.

[22]. Specifically, the surface pressure coefficients at two angles of attack, 4 and 20.18°, respectively, were compared with wind-tunnel acquisitions at the already mentioned freestream flow conditions ($M = 0.197$, $Re = 3.52 \cdot 10^6$).

To this purpose, in MSES a two-dimensional structured grid was generated around the airfoil with an extension of six chord lengths in the chordwise direction and seven chord lengths in the perpendicular direction. A whole of 181 elements were created along the chord of the multi-element airfoil (95 around the slat, 200 over the main airfoil and 135 around the flap) and 42 in the normal direction. A global view and a close-up of the grid used for validation are shown in Fig. 2, where the displacement of the grid clearly depicts the massive flow separation occurring on both the rear of the slat and the main airfoil flap cove.

Regarding simulations carried out in Fluent™, a multiblock 2-D structured grid was created as suggested in [26] (see Fig. 3) mapping a domain of 100 main chord length and height, with the wing in the domain center. A total of 175 grid points were used to describe the slat, while 540 and 188 nodes were adopted for the main and the slat, respectively. The height of the first row from the walls was 8E-6 times the main chord length while the grow rate within the grid boundary layer was fixed at 1.05 for each airfoil element. As a result, y^+ values had average values around 0.63, the maximum being 1.8. The grid configuration resulted from a sensitivity analysis where C_p distributions, as well as global lift, drag, and moment coefficient reached an asymptotic behavior with respect to the node and cell density. In the flow simulations, steady RANS equations were solved using the settings specified in Table 1.

The comparison of computed surface pressure coefficients against experimental results is reported in Fig. 4 for both the simulated incidences using the two codes. Almost independently from the code adopted, a very good agreement of calculated C_p with wind-tunnel data can be observed over the main airfoil and the flap for both $\alpha = 4°$ and $\alpha = 20.18°$; regarding the slat, some major discrepancies are evidenced over the pressure side at $\alpha = 4°$, due to the large flow separation occurring in this region, while correlation keeps satisfactory at $\alpha = 20.18°$. It is worth underlining that, regarding the slat pressure side at $\alpha = 4°$, the k-ω shear stress transport (SST) turbulence model leads to very small improvements in accuracy compared with the inviscid/viscous method implemented in MSES.

Figure 5 shows the computed lift, drag, and moment coefficients compared with the experimental results. Good agreement is obtained for most of the angle-of-attack range. Computations were carried out within the range were MSES code was able to converge, i.e., from −4 to +20°. Outside this range, only Fluent™ was capable to reach convergence (results not shown), since massive separations occurred.

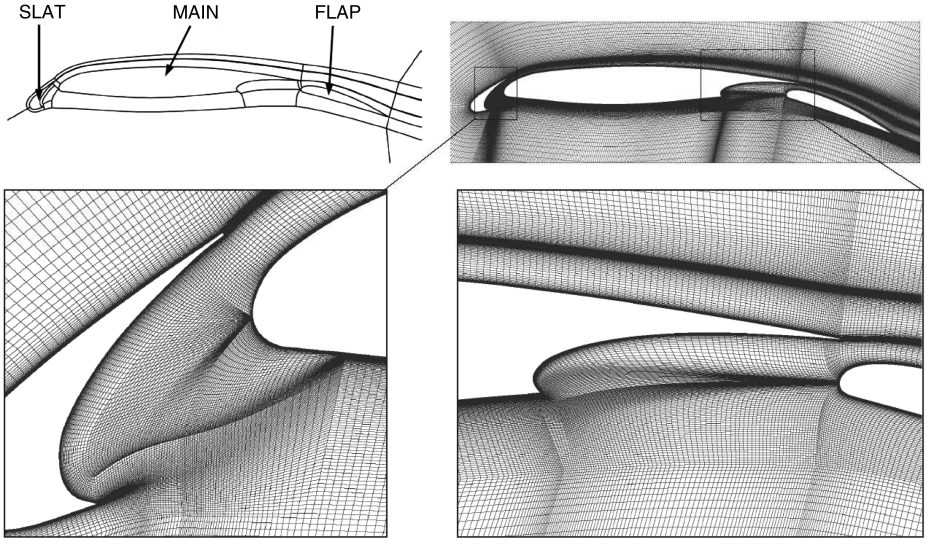

Fig. 3 Domain partition (top left) and close-up views of the grid used.

Table 1 Parameter setting in the CFD simulations

Fluid	Air, ideal gas, Sutherland viscosity model
Turbulence model	k-ω SST with low-Reynolds correction [27]
Turbulence parameters	Turbulent intensity = 4%, turbulent viscosity ratio = 10.
Operating pressure	101325 Pa
Boundary conditions	Far field (Mach, pressure, and temperature specified)
Solution scheme	Coupled
Gradient reconstruction scheme	Green–Gauss node based
Pressure interpolation scheme	Second order
Convective scheme	"Third-order MUSCL" [25]
Convergence criterion	Maximum residual less than 1E-5 or iteration number greater than 1250.

Overall, both codes were satisfactorily accurate in computing lift and drag coefficients for slat-airfoil and airfoil-flap configurations provided that massive flow separations were not reached. Moreover, it is well known that for well-optimized slat-airfoil-flap configurations maximum lift can be achieved without massive flow separations on the wing. Instead, the slat wake merges into the main element boundary layer or wake. For these reasons, and because of its fastness, MSES was selected as the solver to be used in the optimization procedure.

Formulation of the Optimization Problem

The optimization work carried out in this paper was aimed at increasing the aerodynamic performance, i.e., increasing lift for a given drag or decreasing drag for a given lift, of the NHLP 2-D L1T2 high-lift configuration in a multipoint scenario: specifically, the optimal shape and setting of both slat and flap at both T-O and LDG conditions were searched for.

Three variables were used to define each of the leading and trailing-edge devices settings, i.e., their position relative to the main element. In particular, the slat and flap deployment angle, as well as gap and overlap were selected as the design, or decision, variables for setting optimization. The slat deployment angle is defined as the angle between the clean profile chord and rotated chord fixed relative to the slat, while the slat gap is the smallest distance between the deployed device TE and the clean airfoil nose; finally, the slat overlap is expressed as the distance between the vertical tangent to the main element nose and the deployed device TE (top of Fig. 6). The overlap value is here defined positive when the slat TE overlaps the nose and negative when it overcomes the nose LE. Concerning the flap, the deployment angle is identified as the angle between the clean profile chord and rotated chord fixed relative to the flap, while the gap measurement is outlined as the minimum distance between the main element shroud TE and the deployed device. Finally, the flap overlap is defined as the horizontal distance between the deployed device LE and the main element shroud TE, having positive values when the

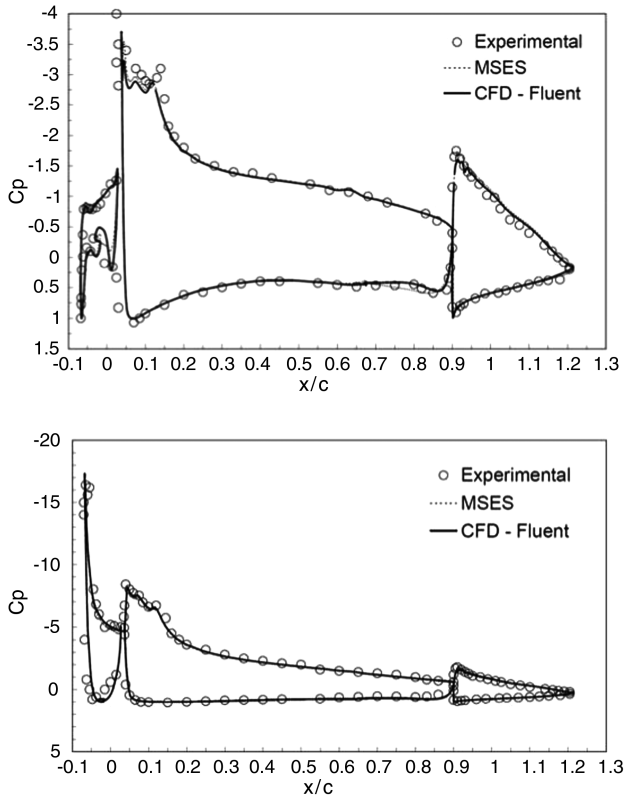

Fig. 4 Pressure coefficient over the NHLP 2-D L1T2 airfoil: comparison of MSES and Fluent™ results with experimental data at an angle of attack $\alpha = 4°$ (top) and $\alpha = 20.18°$ (bottom).

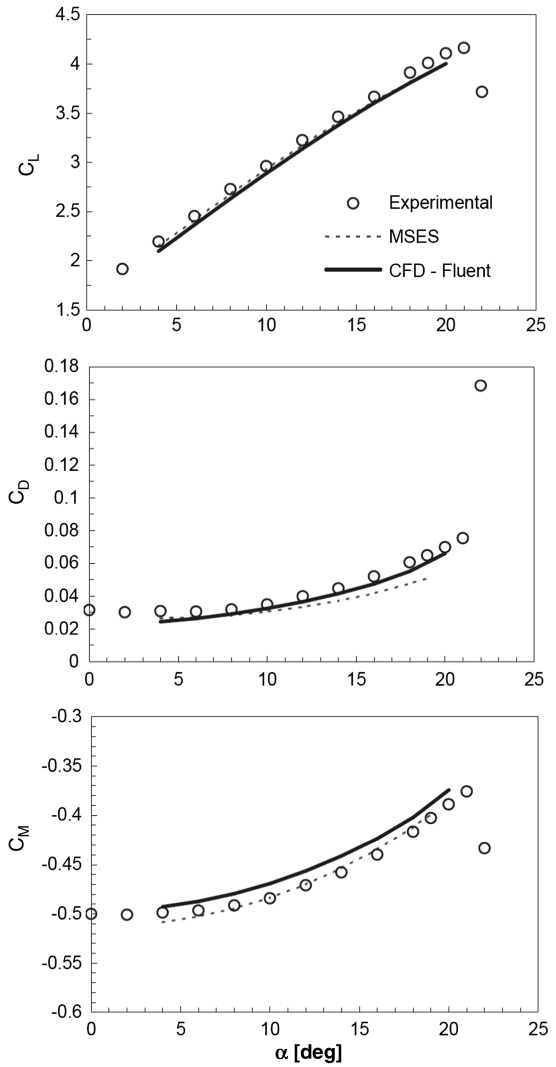

Fig. 5 Overall computed vs experimental lift, drag, and moment coefficients.

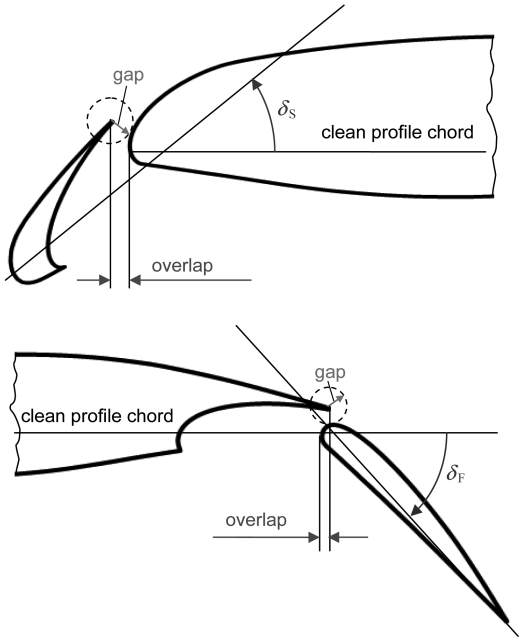

Fig. 6 Slat and flap parameterization (1).

flap LE overlaps the main element shroud and negative values when it moves past the main element shroud TE (bottom of Fig. 6).

Moreover, also the optimal shape of both leading- and trailing-edge devices was parameterized: actually, design modifications of slat and flap could drive the flow behavior and pressure distribution over their surfaces, thus leading to potentially increased overall aerodynamic performance of the multi-element airfoil. In the current optimization problem, only some portions of the slat and flap were subject to shape modifications, as illustrated in Fig. 7: specifically, the optimization was limited to regions of the geometry that are hidden when the airfoil is in the retracted configuration, i.e., the slat lower surface (and the corresponding side in the main element) and the flap suction side (and the corresponding flap shroud in the main airfoil as well). The lower and upper bounds for both the leading and trailing-edge control points (C.P.) are summarized Table 2. A suitable shape parameterization technique should be searched for, making it possible to guarantee smoothness and tangential continuity of the generated shape both at the end points and in between them. In the present paper, a Bézier curve representation of the high-lift devices shape was selected, so that the shape modifications could be carried out manipulating the control points' position over the curves; obviously, the directions of the second and second last C.P.'s movements were constrained by tangency requirements with the unmodified geometry. A whole of five Bézier points were used to define the slat shape, while the flap portion was parameterized using 6 C.P.s: the position of the Bézier points for the original shape of both slat and flap is illustrated in Fig. 7, while their coordinates and ranges are reported in Table 2. A proper variation range was chosen for each of the C.P. position, in order for the explored design space to be satisfactorily large, while keeping the generated shapes close to realistic configurations.

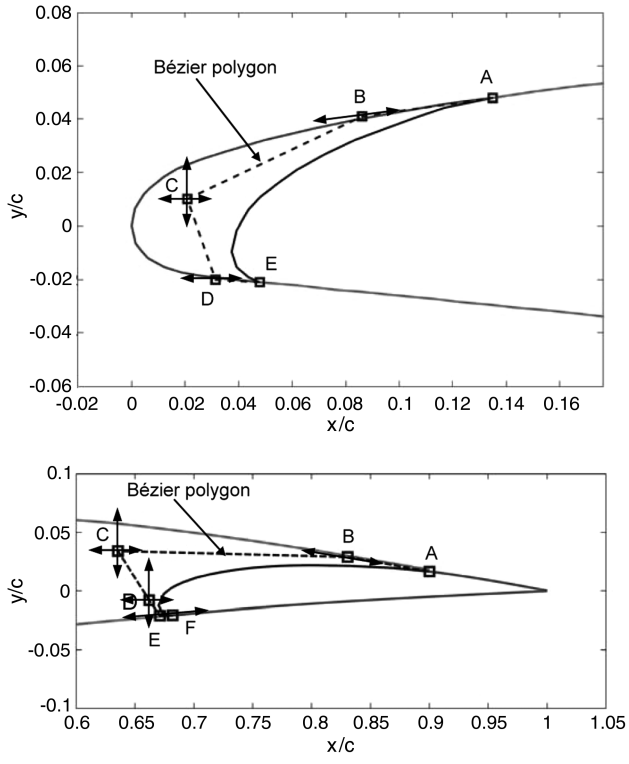

Fig. 7 Slat and flap parameterization (2).

Two configurations, one for T-O and one for LDG conditions, were selected as the baseline for the optimization work: they consisted of the original NHLP 2-D L1T2 shaped multi-element airfoil with high-lift devices deployments typical of the two considered flight conditions, respectively [2]. In particular, the baseline geometries for T-O and LDG configurations were derived from the original retracted airfoil with the combination of setting parameters reported in Table 2. Moreover, incidence angles of 14 and 7 deg were investigated for T-O and LDG conditions, respectively, (as are they linked to the evaluated performance of the baseline airfoil), while the reference flow conditions were those already used for validation of the flow solver ($M = 0.197$, $Re = 3.52 \cdot 10^6$).

As stated above, the optimization work was aimed at improving the aerodynamic characteristics of the multi-element airfoil in both T-O and LDG conditions. The definition of the objective function in T-O was based on the climb index, which is a performance indicator directly correlated to the reduction of the time-to-climb (and therefore fuel burn) at this flight condition [22]. Moreover, it appears particularly suited for high-lift aerodynamic efficiency improvement with respect to the lift-to-drag ratio, in that it introduces an additional weight factor on the lift coefficient. On the other hand, the reduction of fuel burn and noise emissions is one of the primary requirements for high-lift configurations in LDG conditions: this objective can be achieved by minimizing the drag coefficient. It is worth noting, however, that, especially in a 2-D design study, still achieving high-lift coefficients is essential for LDG [28]. This is the reason why an inequality constraint has been considered for the lift coefficient in this condition (see later on).

Therefore, the following two-objective function was identified as the optimization function to be minimized:

$$\mathbf{F} = \begin{cases} F_{\mathrm{TO}} = -\dfrac{C_L^3}{C_D^2}\Big|_{@\alpha=14^\circ} \\ F_{\mathrm{LDG}} = C_D|_{@\alpha=7^\circ} \end{cases} \tag{1}$$

Some constrains have been considered during the optimization process, regarding the aerodynamic characteristics of the final airfoil configurations. The lift coefficient for both the configurations, T-O and LDG, was requested to be greater than or equal to the original values of the baseline:

$$C_{L,\mathrm{TO}} \geq C^*_{L,\mathrm{TO}} \qquad C_{L,\mathrm{LDG}} \geq C^*_{L,\mathrm{LDG}} \tag{2}$$

where $C^*_{L,\mathrm{TO}}$ and $C^*_{L,\mathrm{LDG}}$ are the lift coefficients of the baseline profile and their values are, respectively, 3.555 and 3.359. This constraint was handled using penalty functions as follows:

$$P_{L,\mathrm{TO}} = \begin{cases} 0 & \text{if } C_L \geq C^*_L \\ \beta|C_{L,\mathrm{TO}} - C^*_{L,\mathrm{TO}}|^q & \text{otherwise} \end{cases}$$
$$P_{L,\mathrm{LDG}} = \begin{cases} 0 & \text{if } C_L \geq C^*_L \\ \beta|C_{L,\mathrm{LDG}} - C^*_{L,\mathrm{LDG}}|^q & \text{otherwise} \end{cases} \tag{3}$$

It is worth noting that the penalty function P_L was defined in a general way since it takes the same form for both the configurations.

Table 2 List of design variables and ranges

No.	Design variable	Lower bound	Upper bound	Baseline airfoil
1	I Bézier parameter (SLAT) "B"	0.017078	0.04	0.017078
2	II Bézier parameter (SLAT) "x-C"	0.01	0.020692	0.020692
3	III Bézier parameter (SLAT) "y-C"	0	0.03	0.009885
4	IV Bézier parameter (SLAT) "D"	0.049518	0.08	0.049518
5	I Bézier parameter (FLAP) B	0.01085	0.015	0.01085
6	II Bézier parameter (FLAP) "x-C"	0.65	0.662	0.662
7	III Bézier parameter (FLAP) "y-C"	−0.008	0	−0.008
8	IV Bézier parameter (FLAP) "x-D"	0.6	0.6355	0.6355
9	V Bézier parameter (FLAP) "y-D"	0.034	0.06	0.034
10	VI Bézier parameter (FLAP) "E"	0.07	0.13	0.07
11	Delta slat T-O, deg	17	23	20
12	Gap slat T-O	0.0162	0.0198	0.018
13	Overlap slat T-O	0.0126	0.0154	0.014
14	Delta flap T-O, deg	20	26	23
15	Gap flap T-O	0.0189	0.0231	0.021
16	Overlap flap T-O	0.0324	0.0396	0.036
17	Delta slat LDG, deg	23.5	29.5	26.5
18	Gap slat LDG	0.0198	0.0242	0.022
19	Overlap slat LDG	−0.0198	−0.0162	−0.018
20	Delta flap LDG [deg]	31	37	34
21	Gap flap LDG	0.0144	0.0176	0.016
22	Overlap flap LDG	0.009	0.011	0.01

The penalty coefficient β was set to 1 and the penalty exponent q to 0.85. When the lift of the actual analyzed airfoil is greater than or equal to the original one, no penalty was added to the objectives, otherwise the power function in Eq. (3) was used:

$$\mathbf{F} = \begin{cases} F_{\mathrm{TO}} = -\dfrac{C_L^3}{C_D^2}\Big|_{@\alpha=14^\circ} + P_{L,\mathrm{TO}} \\ F_{\mathrm{LDG}} = C_D|_{@\alpha=7^\circ} + P_{L,\mathrm{LDG}} \end{cases} \tag{4}$$

A second family of constraints concerned the pitching moment coefficient about the quarter-chord point, as the potential excessive increase of the airfoil negative pitching moment was regarded against. In fact, the pitching moment coefficients of new airfoils were allowed to be greater than or equal to 110% of the original values (for both the configurations):

$$C_{m1/4,\mathrm{TO}} \geq 1.1 \cdot C^*_{m1/4,,\mathrm{TO}} \qquad C_{m1/4\mathrm{LDG}} \geq 1.1 \cdot C^*_{m1/4,,\mathrm{LDG}} \tag{5}$$

where the sign is well posed since the moments recognized in these configurations have always negative values. The present constraint was not perceived as strict as the previous one, so a simple a posteriori postprocessing check was made without explicitly adding penalty functions.

To account for the two different operating conditions, i.e., T-O and LDG, proper slat and flap deployment a proper geometric alignment of the devices to the targeted positions had to be dealt with. The effective deployed geometry for each configuration must be calculated considering the particular parameterization technique here employed. The position of each device (i.e., slat and flap) was defined by a deflection (or rotation) relative to the retracted geometry as well as using two coordinates on the section plane. Here we defined the exact methodology to obtain the final deployed geometry from the retracted one, once the geometric parameters are known. Having in mind the definitions of both flap and slap setting parameters, the following procedure was adopted to identify the deployed configuration.

Setting rotation δ was applied first around a fixed point and then displacements Δx and Δy were added to match the imposed gap and overlap values (which were the actual design variables). These deltas were calculated firstly by applying the overlap (it can be calculated directly from the coordinates to find the Δx) and then the gap. The latter was found using an iterative approach, i.e., by moving vertically the device using very small spatial steps until Δy was calculated with a geometric tolerance of $10^{-7}c$. The angle and the plane deltas were finally applied to the device geometry as follows:

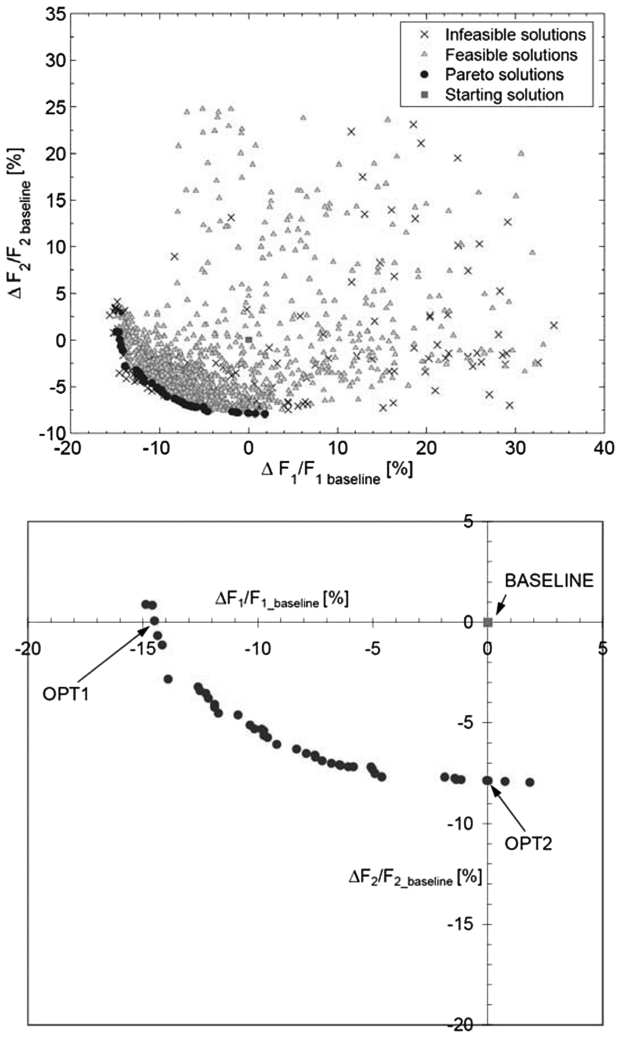

Fig. 8 Final Pareto front. Overall view including all individuals (top) and close up (bottom).

Table 3 Pareto optimal design variable values for optimized solutions

No.	Design variable	OPT1 airfoil	OPT2 airfoil	Baseline airfoil
1	I Bézier parameter (SLAT)	0.0254	0.0248	0.017078
2	II Bézier parameter (SLAT)	0.0198	0.0192	0.020692
3	III Bézier parameter (SLAT)	0.0045	0.0068	0.009885
4	IV Bézier parameter (SLAT)	0.0550	0.0717	0.049518
5	I Bézier parameter (FLAP)	0.0114	0.0120	0.01085
6	II Bézier parameter (FLAP)	0.6587	0.6589	0.662
7	III Bézier parameter (FLAP)	−0.0061	−0.0054	−0.008
8	IV Bézier parameter (FLAP)	0.6308	0.6273	0.6355
9	V Bézier parameter (FLAP)	0.0447	0.0458	0.034
10	VI Bézier parameter (FLAP)	0.0987	0.0952	0.07
11	Delta slat T-O, deg	18.24	18.47	20
12	Gap slat T-O	0.0175	0.0179	0.018
13	Overlap slat T-O	0.0136	0.0143	0.014
14	Delta flap T-O , deg	21.89	21.77	23
15	Gap flap T-O	0.0212	0.0217	0.021
16	Overlap flap T-O	0.0355	0.0344	0.036
17	Delta slat LDG, deg	25.47	24.4	26.5
18	Gap slat LDG	0.0213	0.0213	0.022
19	Overlap slat LDG	−0.0179	−0.0176	−0.018
20	Delta flap LDG, deg	32.82	31.82	34
21	Gap flap LDG	0.0159	0.0154	0.016
22	Overlap flap LDG	0.0099	0.0095	0.01

$$x_{\text{dep}}(\delta) = x_0 + (x - x_0)\cos(\delta) - (y - y_0)\sin(\delta) + \Delta x$$
$$y_{\text{dep}}(\delta) = y_0 + (x - x_0)\sin(\delta) + (y - y_0)\cos(\delta) + \Delta y \quad (6)$$

where x_0 and y_0 are the coordinates of the rotation center, invariantly positioned at $x_0[x/c] = 0.135$ and $y_0[y/c] = 0.048$ for the slat and at $x_0[x/c] = 0.9$ and $y_0[y/c] = 0.0179$ for the flap. Equation (6) was used without distinction for both the devices.

Optimization Methodology

A state-of-the-art MOGA was used for handling the optimization problem [27]. As it widely known, MOGAs are algorithms that reproduce the behavior of adaptive systems present in nature. An initial population of individuals (each one represented by numerical parameters), is evaluated providing their solutions. The most attractive individuals, selected in proportion to their fitness, are used to produce offspring through recombination; mutations are finally applied to ensure the probability of small and casual modifications on genes. The procedure continues until convergence or maximum number of generation is reached. The benefits of MOGAs for optimization problems have been extensively documented [27,29], the most important relying in their multi-objective nature, their good behavior with highly multimodal functions, and inclination to parallelization.

MATLAB® R2008b environment [30] offers a general version of a MOGA (available using *gamultiobj* function of Genetic Algorithm and Direct Search Toolbox™), widely derived from [27]. Although it has not been created expressly for aerodynamic problems, it is fully customizable. It offers a large number of options regarding crossover

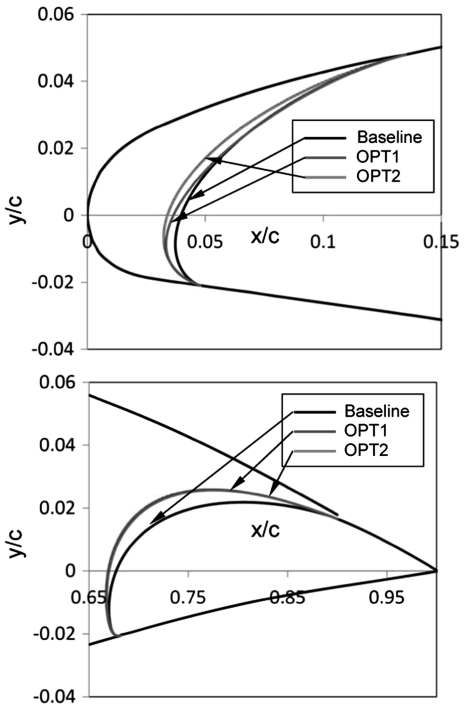

Fig. 9 Optimized slat and flap shapes in retracted configuration (axes out of scale).

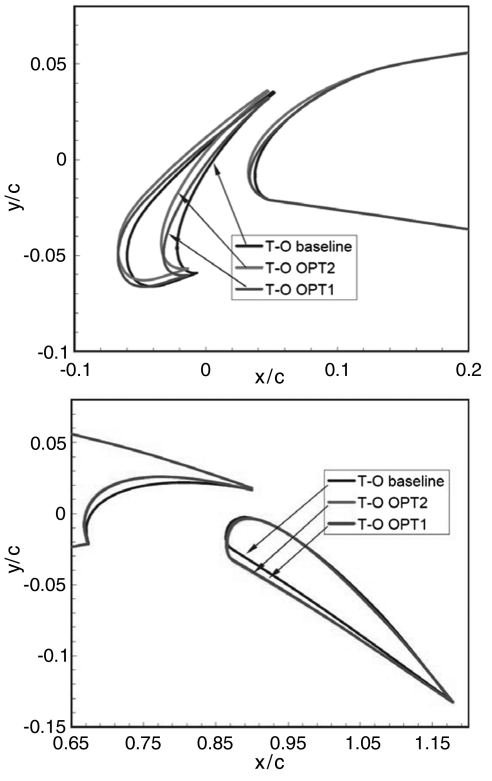

Fig. 10 Optimized slat and flap configurations for takeoff.

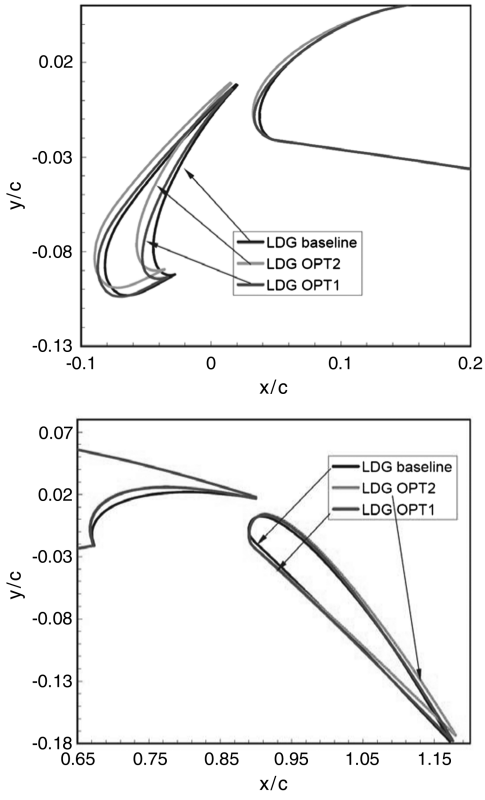

Fig. 11 Optimized slat and flap configurations for landing.

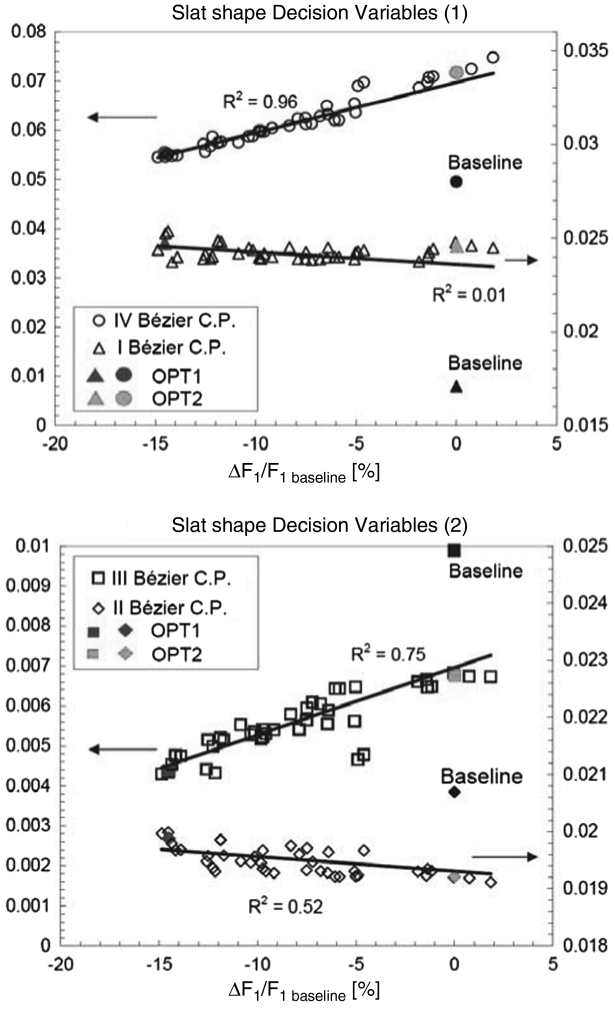

Fig. 12 Slat shape: analysis of optimal parameters.

and mutation probability, population type, and selection methods, providing a flexible solution.

The first option considered is the coding method in which the algorithm treats the free variables. Given the nature of the parameterization used here, we set a real number coding. The algorithm offers different ways to scale the individuals in each generation in proportion to their scores, and a typical rank method is chosen, so the rank of the fittest individual is 1, the next fittest is 2, and so on. This kind of fitness scaling technique removes the effect of the spread of the raw scores. Once the scores have been assigned to each individual, two parent populations are created to produce children by

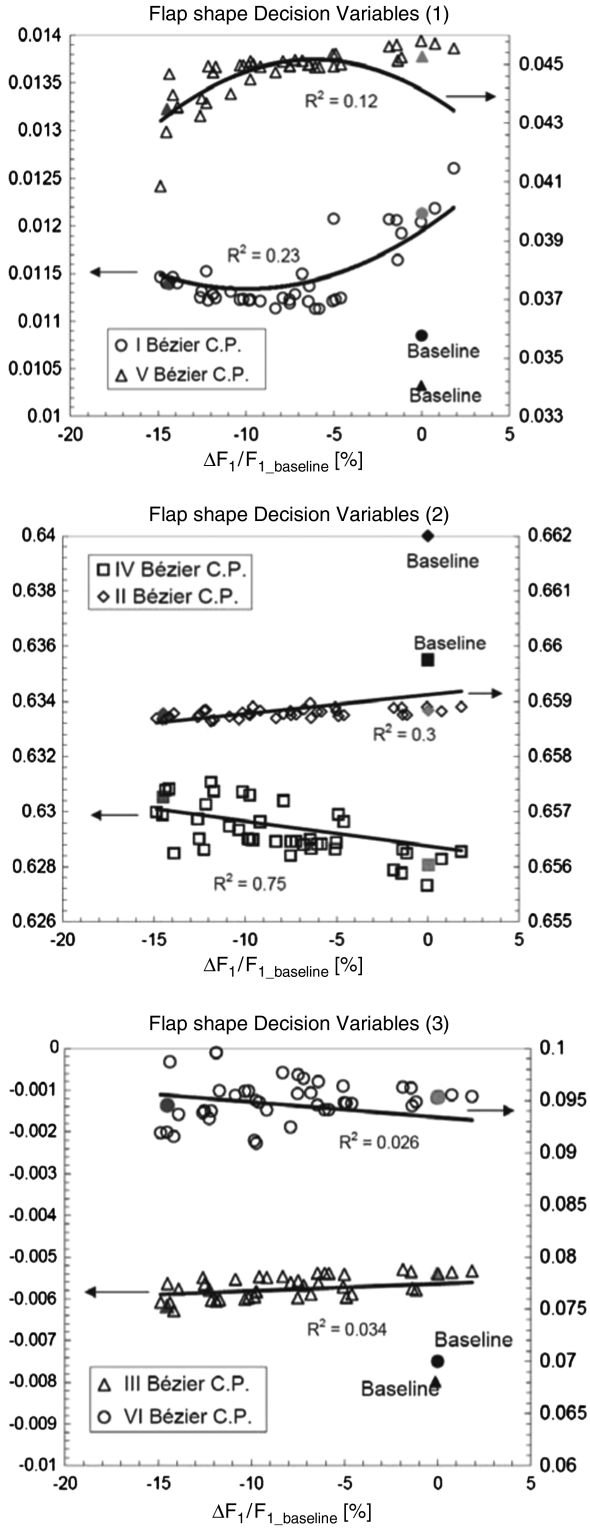

Fig. 13 Flap shape: analysis of optimal parameter.

crossover. The stochastic uniform selection was used during the present optimization. A cumulative probability vector was created from the previous rank and the parents were selected stochastically, according to their own probability. Finally, the two parent populations were combined together to generate children using a scattered method to perform the crossover. A random binary vector (with a length equal to the number of free variables) is created and the genes corresponding to 1 values are selected from the individual of the first parent population, while the genes corresponding to 0 values are selected from the same individual of the second parent population. This operation is performed until a new complete population is created. Mutation and elitism were also used here. We specified an elite individual number equal to 2, so there were 2 individuals of the actual generation that are guaranteed to survive to the next one. The remaining children were then divided into two groups; the individuals in the first group were generated by crossover (as previously explained) and the individuals in the second one by mutation. Mutation provided genetic diversity and enabled the MOGA to search in a broader space. It was applied using a Gaussian technique that adds a random number, taken from a Gaussian distribution with mean 0, to the parent individuals.

Finally, the population size was chosen multiplying the number of free variables (equal to 22) by a factor of 3 or 4 [27]. The value of 70 individuals per generation felt within the cited interval. The total number of generations performed was set to 30 artificially, corresponding to 2100 evaluations of the fitness function.

Results and Discussion

On top of Fig. 8, the final Pareto front, i.e., those individuals that are optimal according to the Pareto optimality criterion, is shown where the variations in the two objectives with respect to the baselines are reported along the axes. In this figure, the point located at (0,0) and highlighted in red is therefore representative of the initial solution while those marked in black belong to the Pareto front. All the solutions found by the algorithm during the search are depicted as well in this figure, such that an immediate view of both feasible and infeasible solutions is possible. To this respect, it is worth recalling that infeasible solutions are those which do not respect the constraint either given by Eqs. (2), (3), and (5). A closer view of the Pareto front is given in the bottom part of Fig. 8, where a quantitative measure of fitness for best individuals is also possible. In particular, solutions named "OPT1" and "OPT2" are of primary importance, since they qualify the improvements in one objective while the other is kept fixed. OPT1 is therefore the individual which, at T-O, dominates the initial solution in terms of C_L^3/C_D^2 (in fact almost a 15% reduction is registered) while keeping, at LDG, the same drag coefficient. On the other hand, OPT2 assures an 8% reduction in the drag coefficient at LDG while maintaining the same C_L^3/C_D^2 at T-O.

The shape of the Pareto front demonstrates that a conflict does exist between the two objectives, thus suggesting that different optimal airfoil shape having different settings can be found which maximize airfoil performance into two operating conditions.

Table 3 reports the Pareto optimal set, where the values for the optimized design variables are reported and compared with the baseline's. A graphical representation of the two optimized geometries, in both T-O and LDG conditions, as well as in retracted configuration, is therefore given in Figs. 9–11. While almost only a qualitative discussion about these results is possible, it is worth underlying that some significant differences exist among the profiles' shapes and settings which lead to better performance, as clarified below.

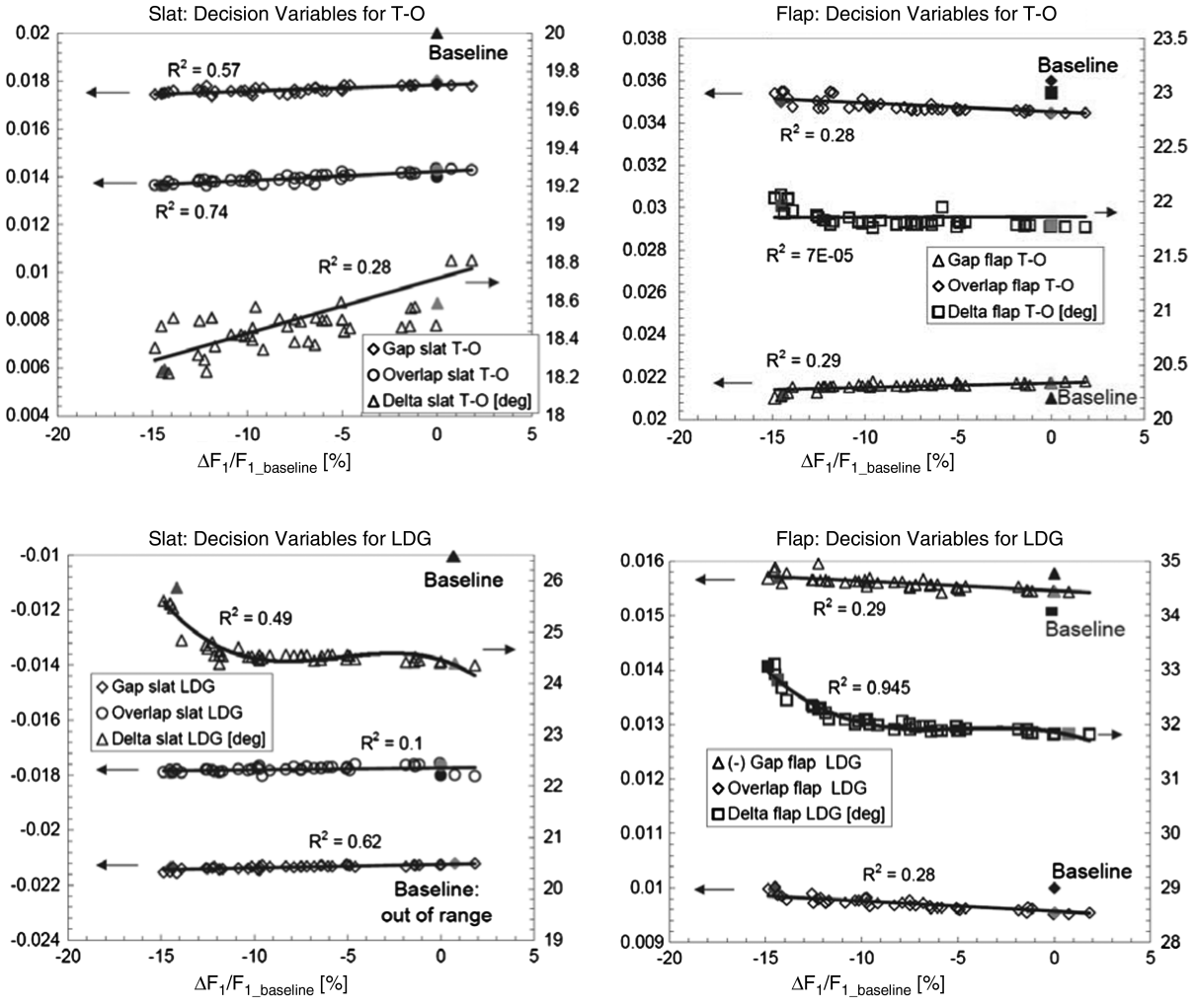

Fig. 14 Slat and flap settings: analysis of optimal parameters.

First of all, we must examine where the position of the optimized solutions is with respect to the assumed search space and Pareto front. This is done to assess both: 1) whether or not variations leading to optimal individuals correctly fall within the search space, i.e., whether or not the amplitude of the design variables interval is correctly set; and 2) whether or not optimal values for the design variables belonging to the Pareto optimal set, in particular OPT1 and OPT2, correlate with each other and exhibit a certain tendency, such that an optimality criterion can be argued or even statistically formulated via a variance analysis.

To answer the first issue we simply examine Tables 2 and 3, in which the ranges for each design variable are given. Some Bézier parameters for both slat and flap are limited by side constraints to which the optimal solutions must conform. Actually, optimal Bézier parameters for both the slat and the flap shape (10 parameters in total) fall well inside the given allowable ranges, indicating that optimal shapes for OPT1 and OPT2 are captured. As a general remark, from Tables 2 and 3, as well as from Figs. 10 and 11, we can notice that the slat shape of optimal solutions does not change very much with respect to the baseline, both in T-O and LDG conditions.

As far as the remaining design variables (from #11 to #22) are concerned, the same conclusions can be drawn regarding ranges amplitude appropriateness, such that also the components' setting is adequately optimized.

A couple of major aspects are, however, preliminarily evidenced here regarding the optimal solutions OPT1 and OPT2. In fact, the optimal flap shape is thicker compared with the baseline, exhibits a well-rounded nose and a fairly similar series of setting parameters at T-O, a feature which makes it possible to maintain high lift while minimizing drag properties, as will be more deeply described later on. In the LDG phase, on the other hand, where only the drag is accounted for, the flap settings is significantly changed: in particular Delta flap LDG, i.e., the setting angle, is reduced so as to minimize drag by delaying boundary-layer transition (this aspect will be more clear afterward). Also this aspect, indeed quite relevant, will be much more clear afterward, where boundary-layer properties will be analyzed.

The existence of a correlation among design variables of optimal airfoils can be discussed by examining plots from Figs. 12–14. In such figures, the values of the 22 design variables of optimized airfoils are represented against the relative values of the first objective. Since similar plots are uniquely derived from such data and the Pareto front for the second objective, these charts can be used to analyze relationships between design variables and objectives without any lack of generality. To support such analysis, the values of the correlation coefficient R^2 were calculated and reported as well.

As a general comment, only few optimal design variables are actually correlated, and a different behavior is registered for the flap and the slat. This means that, as a rule of thumb, no general and rigorous optimality rule based on elementary statistics can be extracted for both the airfoil components. Nevertheless, some useful comparison with the baseline variables can be drawn. Moreover, as far as the slat shape is concerned, more convincing arguments supporting the idea of a more general optimization criterion can be offered, as better specified below.

Optimal Slat Parameters

From top of Fig. 12 we may see that the fourth Bézier variable for the slat shape (corresponding to point B in Fig. 7 top) is always greater than the baseline's and that is very well correlated with the objective ($R^2 = 0.96$), thus inducing to argue that optimal slat shapes must always have a slightly thicker TE compared with the starting airfoil. This conclusion is in fact correct from the statistical viewpoint, but the circumstances which led to it may be fortuitous, as the authors suspect, since no clear evidence of flow improvement is attributable to the slat shape independently from its setting. In other words, at least in this study, it is not possible to distinguish between improvements due to the different slat TE and those related to different slat settings, as these changes occur simultaneously.

Moving to the other slat shape parameters (from point C to point D in Fig. 7 top), correlation becomes progressively weaker but is still significant. Optimal values of ordinates for C (III Bézier C.P.) indicate that good correlation exists ($R^2 = 0.75$) and that those values are always lower than the baseline's. However, such fact contrasts with the resulting always lesser values of optimal abscissas for C (the greater dispersion, $R^2 = 0.52$, does not affect such unique behavior). As a result, optimal slat shape in the middle chord is not very much different with respect to the baseline's.

Regarding the position of point D (I Bézier C.P.), data of optimized configurations is completely uncorrelated ($R^2 = 0.01$) even though fairly thicker slat LEs compared with the baseline's are always perceived as best.

Slat setting parameters play an important role in understanding the phenomenon being studied. The left-hand side of Fig. 14 shows optimal values for slat setting design variables in both T-O and LDG phases. While both optimal gap and overlap values are very close to those of the starting profile and both exhibit satisfactory correlation against objectives (at least three out of four: $R^2 = 0.74$ overlap, $R^2 = 0.57$ gap at T-O; $R^2 = 0.1$ overlap, $R^2 = 0.62$ gap at LDG), values of slat setting angle are apparently lower, while showing a relatively modest correlation: $R^2 = 0.28$ at T-O and $R^2 = 0.49$ at T-O.

As a matter of fact, this makes it possible to increase slat lift during T-O and decrease its drag at LDG.

In fact, from top of Fig. 15 a lower peak in the C_p distribution is found in OPT1 suggesting the occurrence of a slightly higher actual angle of attack, with respect to the deployed slat chord, which ultimately leads to a higher slat lift at T-O. On the other hand, from top of Fig. 15, a localized but significant reduction in the C_p is registered at the main LE of OPT1, located on the suction side, which

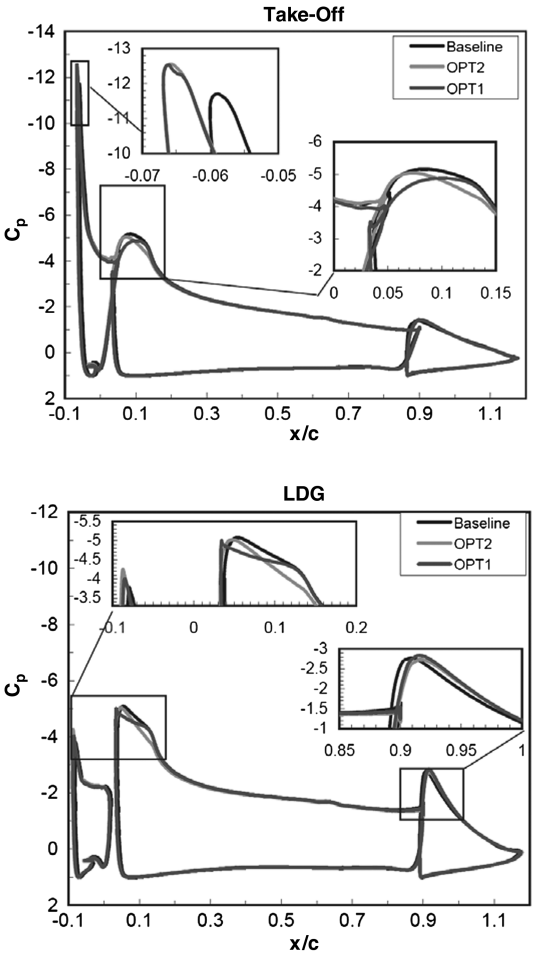

Fig. 15 Cp distribution over baseline and optimized profiles in both takeoff (top) and landing (bottom).

slightly downloads the main airfoil. This loss of lift is, however, compensated by a contextual decrease in the profile drag over both the slat and the main profile. In fact, from Fig. 16 (top and middle), lower values of the skin friction coefficient (SFC) are found in OPT1 both toward the rear of the slat and close to the LE of the main profile.

In LDG conditions, OPT2 slat configuration contributes to maintain the same C_D^2/C_L^3 as the baseline's but the drag coefficient is lower. In fact, from bottom of Fig. 15, a loss of lift is visible in the zoom focusing on the C_p distribution, especially close to the main LE, while a reduction in the drag is expected due to a slightly more favorable distribution of the SFC over the suction side of the main airfoil (see blue curve in Fig. 17 middle).

Optimal Flap Parameters

Overall, shape parameters for the optimized flap are scarcely correlated with objectives (see Fig. 13). The tendency curves at the top of the figure are not given with the purpose of producing a realistic fitting, but rather to highlight great variance of data. If data was fitted using a linear regression model, even lower values of the correlation coefficient would be obtained.

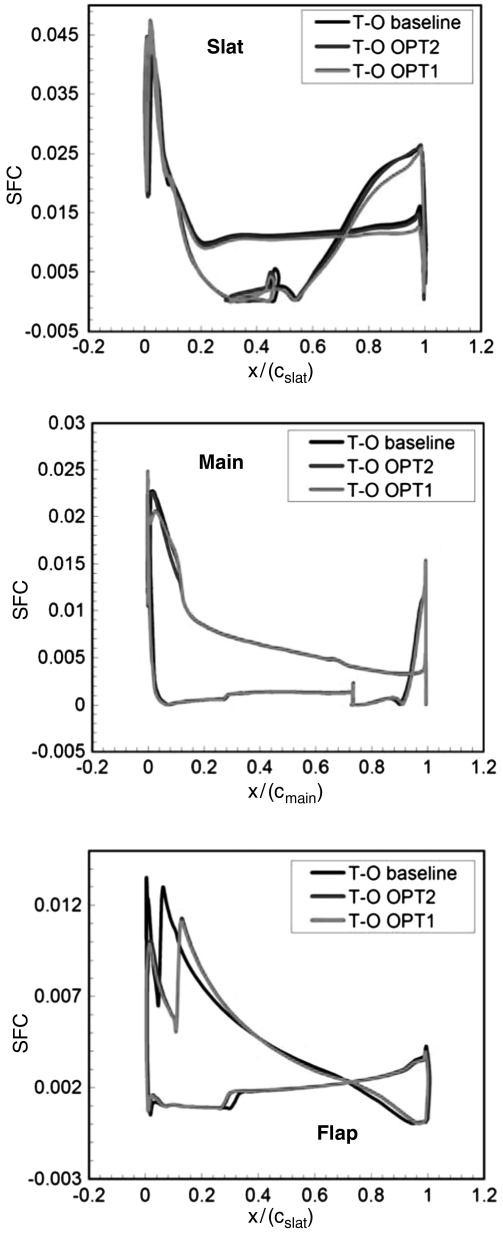

Fig. 16 Skin friction coefficient distribution over baseline and optimized profiles in takeoff.

Despite this, a clear indication of optimality per se is achieved from such plots. In fact, from Fig. 13 we may see that I, III, V and VI Bézier variables for the optimal flap shapes are always greater than the baseline's while II and IV are always lower. Considering the relative weights of such parameters on the flap shape and their distance between baseline's and optimized ones' this means that, as it clearly appears from bottom of Figs. 7 and 10, OPT1 and OPT2 configurations, as well all the others lying on the Pareto front, always have significantly thicker airfoils in the LE region. Moreover, a more pronounced curvature change is found on the flap pressure side, a phenomenon which is likely to be a direct consequence of the constraints imposed on the flap shape and its cove. Contrary to the slat, here the effects of the airfoil shape modifications are much more decipherable, in that a thicker flap profile provides, if correctly set both in T-O and LDG, the required lift at a minimum drag, as better explained below. For now, if we add these considerations to those given in the previous paragraph, it is worth stating that overall we get optimized multi-element airfoils which, compared with the baseline, lead in fact to higher lift and lower drag at T-O as well as a much lower drag in LDG.

In particular, when T-O conditions are considered, i.e., when we look at OPT1 solution mostly, a thicker flap featuring a lower value of the setting angle (approximately 22° compared with about 23° of the starting configuration, see the right-hand side of Fig. 14) with similar

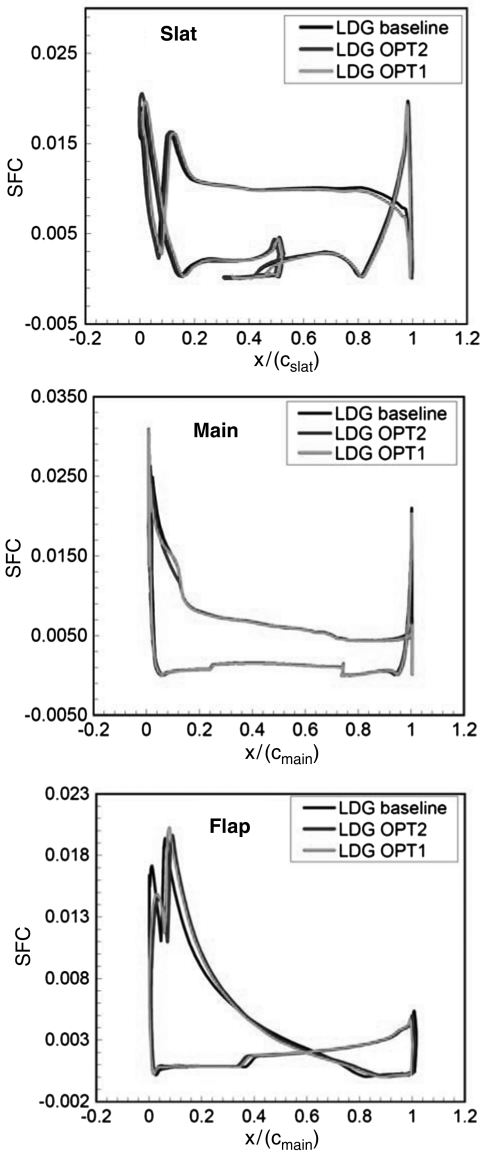

Fig. 17 Skin friction coefficient distribution over baseline and optimized profiles in landing.

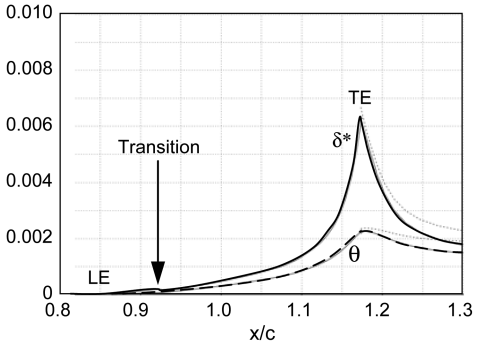

a) T-O, baseline

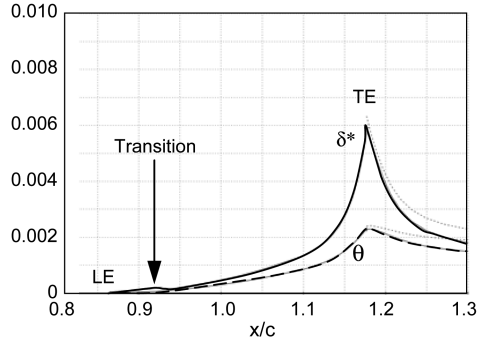

b) T-O, OPT1

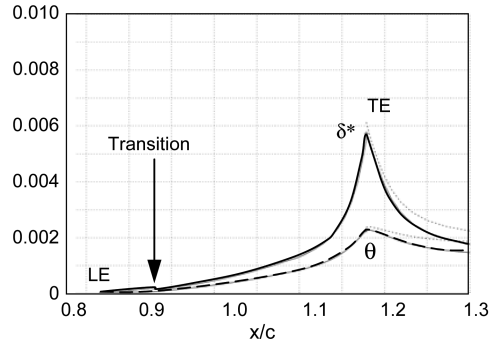

c) T-O, OPT2

Fig. 18 Computed nondimensional boundary-layer displacement and momentum thicknesses.

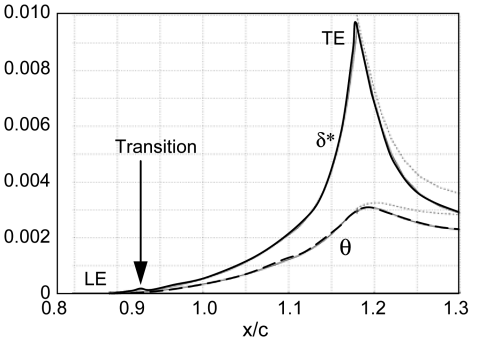

a) LDG, baseline

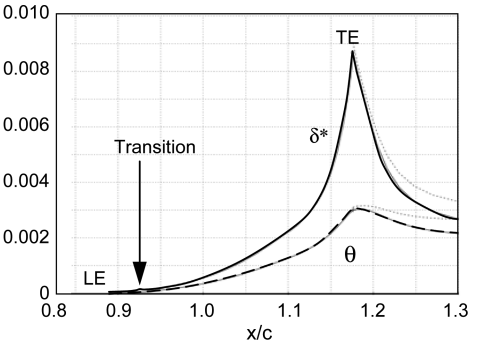

b) LDG, OPT1

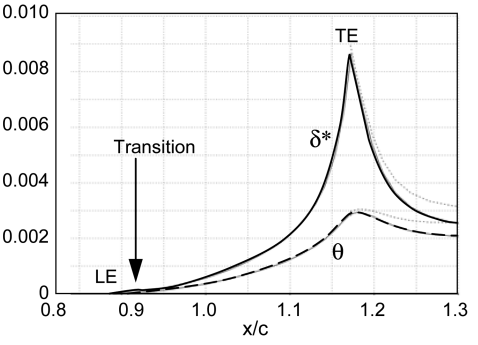

c) LDG, OPT2

Fig. 20 Computed nondimensional boundary-layer displacement and momentum thicknesses.

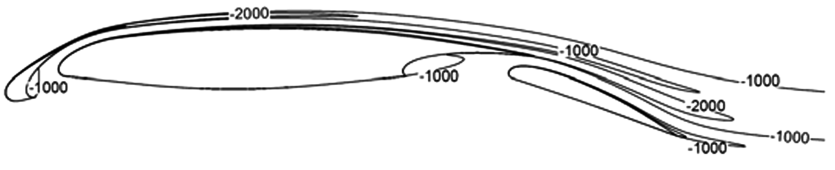

a) T-O, baseline

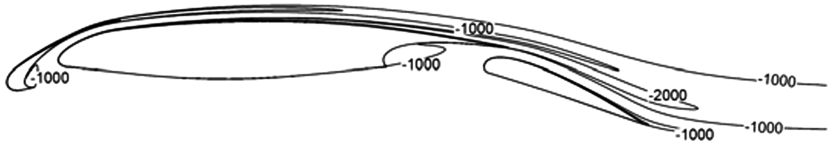

b) T-O, OPT1

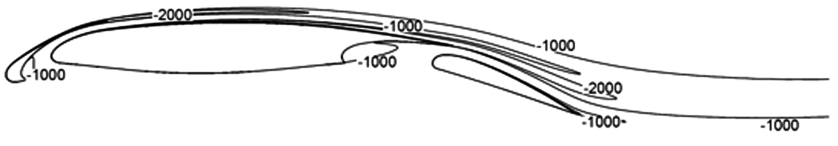

c) T-O, OPT2

Fig. 19 Computed total pressure contours [Pa] relative to the ambient (=0 Pa) at T-O for baseline and optimized configurations.

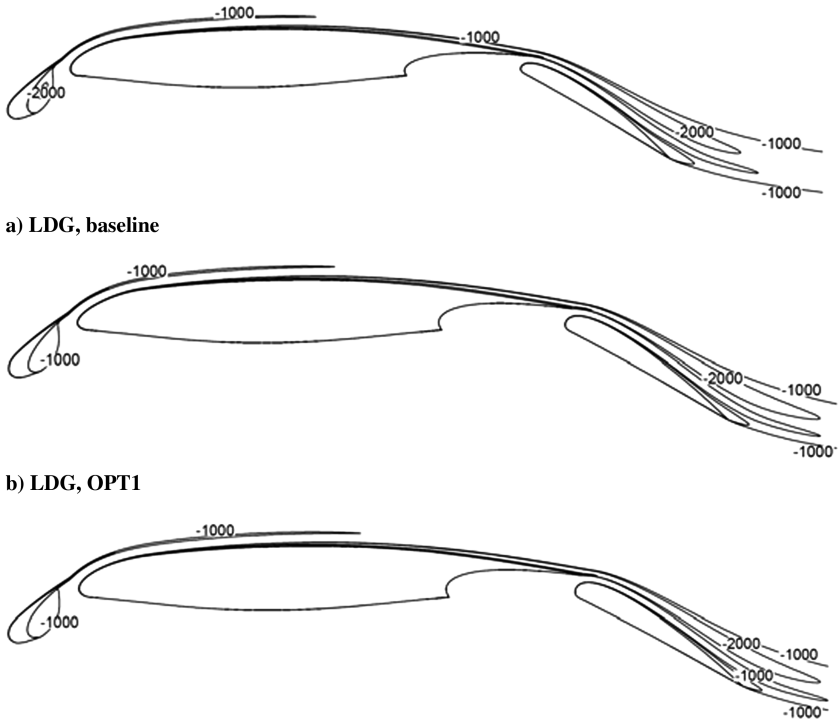

a) LDG, baseline

b) LDG, OPT1

c) LDG, OPT2

Fig. 21 Computed total pressure contours [Pa] relative to the ambient (=0 Pa).

gap and overlap is always able to produce the desired lift in a more efficient manner. In fact, while the C_p distribution over the flap remains virtually unchanged (top of Fig. 15), the SFC (bottom of Fig. 16) clearly shows a reduction in the friction drag, especially over the suction side. In fact, thanks to the capabilities of the turbulence model used in the CFD simulations using Fluent^{TM} (k-ω SST with low Reynolds correction), the distribution of SFC perhaps suggests a postposition in the laminar-turbulent transition. From this point of view, it is worth recalling that the mentioned SST model blends a high-Reynolds k-ε model with a low-Reynolds k-ω model [27]. Therefore, in spite the SST model does not need a further low-Reynolds correction, the model implemented in Fluent^{TM} can predict, using the "transitional flow" option activated, laminar-turbulent transition [25].

This conclusion is confirmed also by analyzing the distribution of the nondimensional boundary-layer properties obtained using MSES (see Fig. 18), where the displacement thickness of OPT1 exhibits a local maximum, close to the flap LE, which is located slightly more downstream compared with the baseline. Moreover, both displacement and momentum thicknesses at the flap TE are lower in the OPT1 configuration: this fact gives reason for lower flap wake drag also. In fact, from Figs. 19a and 19b the contour plots of the relative total pressure around the airfoil show a slightly narrower flap wake in OPT1 compared with the baseline.

In the LDG phase, most of the arguments given above apply as well regarding the OPT2 solution. In this case, however, the thicker flap is set in a different way compared with T-O (see bottom right-hand side of Fig. 14) and the optimal solutions do correlate better with the objectives, giving more emphasis to a so-called general optimization rule ($R^2 = 0.28$ overlap, $R^2 = 0.29$ gap, and $R^2 = 0.945$ setting angle). As a matter of fact, the flap setting angle is a couple of degrees lower than the original one, a fact which ultimately leads to a significant reduction in the flap drag while preserving its lift. In fact, from the bottom of Fig. 15 no substantial differences in the C_p distribution are registered on the flap; despite higher average values of SFC (see bottom of Fig. 17) a postposition in the laminar-turbulent transition (again see the bottom of Figs. 17, 20a, and 20c, lower values of displacement and momentum thicknesses, as well as a slightly narrower flap wake is found (see Figs. 21a and 21c).

Conclusions

In this paper, a two-objective approach for a three-element airfoil was implemented to handle a multipoint constrained problem, where the first and the second objectives were formulated so as to maximize airfoil performance in both T-O and LDG operations. To this purpose, the shape and setting parameters for both slat and flap were taken into account in the optimization, which was dealt with using a MOEA.

Results established that a conflict exists between the two objectives, i.e., confirming the opposing nature of profile performance in the two conditions. Nevertheless, the Pareto optimal set demonstrated that an optimal airfoil shape can be found that maximized airfoil performance by properly changing its setting. This result is quite interesting in that it demonstrates that the multi-element airfoil design contextually involves both shape and setting variables.

Postprocessing of results revealed that:

1) Optimal values for the design variables belonging to the Pareto optimal set, in particular those referred to OPT1 and OPT2 configurations, partially correlate with each other and exhibit a certain tendency, such that an optimality criterion can be argued.

2) In particular, regarding the slat shapes, these must always have a slightly thicker TE compared with the starting airfoil, while in the middle chord these are not very much different with respect to the baseline's. Finally, fairly thicker LEs are always perceived as best, even if Pareto optimal data shows a poor correlation with each other against the objectives. As far as the slat setting is concerned, both optimal gap and overlap values are very close to those of the starting profile and both exhibit satisfactory correlation against objectives, a fact which makes it possible to increase lift-to-drag ratio during T-O and decrease drag at LDG.

3) When flap parameters are examined, a poor correlation with objectives was also observed regarding both its shape and setting parameters. However, a clear indication for optimality could be extracted. In fact, optimal flaps always had thicker airfoils in the LE region and more pronounced curvature on the pressure side. This, along with the occurrence of a lower value for the setting angle, assured higher lift and lower drag at T-O, as well as a much lower drag in LDG.

References

[1] Flaig, A., and Hilbig, R., "High-Lift Design for Large Civil Aircraft," *High-Lift System Aerodynamics*, AGARD CP-515, Neuilly-sur-Seine, France, 1993.

[2] van Dam, C. P., "The Aerodynamic Design of Multi-Element High-Lift Systems for Transport Airplanes," *Progress in Aerospace Sciences*, Vol. 38, No. 2, 2002, pp. 145–180. doi:10.1016/S0376-0421(02)00003-9

[3] Rudolph, P. K. C., "HighLift Systems on Commercial Subsonic Airliners," NASA Contractor Rept. 4746, Sept. 1996.

[4] Meredith, P. T., "Viscous phenomena affecting high-lift systems and suggestions for future CFD development," AGARD CP 315, 1993, pp. 19-1–19-8.

[5] Perraud, J., Cliquet, J., Houdeville, R., Arnal, D., and Moens, F., "Transport Aircraft Three-Dimensional High-Lift Wing Numerical Transition Prediction," *Journal of Aircraft*, Vol. 45, No. 5, 2008, pp. 1554–1563. doi:10.2514/1.32529

[6] Smith, A. M. O., "High-Lift Aerodynamics," *Journal of Aircraft*, Vol. 12, No. 6, 1975, pp. 501–530. doi:10.2514/3.59830

[7] Rumsey, C. L., and Ying, S. X., "Prediction of High Lift: Review of Present CFD Capability," *Progress in Aerospace Sciences*, Vol. 38, No. 2, 2002, pp. 145–180. doi:10.1016/S0376-0421(02)00003-9

[8] King, D. A., and Williams, B. R., "Developments in Computational Methods for High-Lift Aerodynamics," *The Aeronautical Journal*, Vol. 92, No. 917, 1988, pp. 265–288.

[9] Kusunose, K., Wigton, L., and Meredith, P., "A Rapidly Converging Viscous/Inviscid Coupling Code for Multielement Airfoil Configurations," AIAA Paper 91-0177, 1991.

[10] Drela, M., "Newton Solution of Coupled Viscous/Inviscid Multielement Airfoil Flows," AIAA Paper 90-1470, June 1990.

[11] Cebeci, T., "Calculation of Multielement Airfoils and Wings at High Lift: High-Lift System Aerodynamics," AGARD CP 515, Sept. 1993, pp. 24–1–24–15.

[12] Eyi, S., Lee, K. D., Rogers, S. E., and Kwak, D., "High-Lift Design Optimization Using the Navier–Stokes Equations," *27th Fluid Dynamics Conference*, AIAA Paper 1996-1943, June 1996.

[13] Besnard, E., Schmitz, A., Boscher, E., Garcia, N., and Cebeci, T., "Two-Dimensional Aircraft High Lift System Design and Optimization," *36th AIAA Aerospace Sciences Meeting and Exhibit*, AIAA Paper 98-0123, 1998.

[14] Kim, S., "Design Optimization of High-Lift Configurations Using a Viscous Adjoint-Based Method," Ph.D. Dissertation, Stanford Univ., Palo Alto, CA, 2001.

[15] Nemec, M., Zingg, D. W., and Pulliam, T. H., "Multi-Point and Multi-Objective Aerodynamic Shape Optimization," *9th AIAA/ISSMO Symposium on Multidisciplinary Analysis and Optimization*, AIAA Paper 2002-5548, Sept. 2002.

[16] Nakayama, H., Kim, H.-J., Matsushima, K., Nakahashi, K., and Takenaka, K., "Aerodynamic Optimization of Multi-Element Airfoil," *44th AIAA Aerospace Sciences Meeting and Exhibit*, AIAA Paper 2006-1051, Jan. 2006.

[17] Yiju, D., Zhuoyi, D., and Hao, Z., "Aerodynamic Optimization of Multi-Element Airfoils by Genetic Algorithms," *West-East High Speed Flow Field Conference*, Moscow, Russia, Nov. 2007.

[18] Onate, E., Bugeda, G., Zhili, T., and Periaux, J., "Multi-Element Airfoil Lift Maximization Problems with Uncertainties Using Evolutionary Optimization and Unstructured Meshes," *European Conference on Computational Fluid Dynamics*, edited by P. Wesseling, E. Oñate, and J. Périaux, ECCOMAS, Barcelona, 2008.

[19] Lee, Y.-T., Ahuja, V., Hosangadi, A., and Ebert, M., "Shape Optimization of a Multi-Element Foil Using an Evolutionary Algorithm," *Journal of Fluids Engineering*, Vol. 132, Issue 5, May 2010, pp. 051401–051412. doi:10.1115/1.4001343

[20] Greenman, R. M., and Roth, K. R., "Minimizing Computational Data Requirements for Multi-Element Airfoils Using Neural Networks," *Journal of Aircraft*, Vol. 36, No. 5, 1999, pp. 777–84. doi:10.2514/2.2533

[21] Quagliarella, D., "Airfoil Calculations in High-Lift Conditions Using the MAVIAN Program," Centro Italiano Ricerche Aerospaziali, Technical Note CIRA-TN-98-124, Capua, Italy, Dec. 1998.

[22] Wild, J., Brezillon, J., Amoignon, O., Quest, J., Moens, F., and Quagliarella, D., "Advanced High-Lift Design by Numerical Methods and Wind Tunnel Verification Within the European Project Eurolift II," *Journal of Aircraft*, Vol. 46, No. 1, Jan.–Feb. 2009, pp. 526–541. doi:10.2514/1.37148

[23] Drela, M., "Design and Optimization Method for Multielement Airfoils," AIAA Paper 93-0969, Feb. 1993.

[24] Drela, M., "A User's Guide to MSES 2.92," MIT Computational Aerospace Science Laboratory, Cambridge, MA, Feb. 1996.

[25] http://www.fluent.com/

[26] De Rango, and Zingg S. D. W., "Higher-Order Aerodynamic Computations On Multi-Block Grids," *15th AIAA Computational Fluid Dynamics Conference*, AIAA Paper 2001-2631, 2001.

[27] Deb, K., *Multi-Objective Optimization Using Evolutionary Algorithms*, Wiley, New York, 2001.

[28] Kuhlman, W. H., "The Douglas double-slotted flap," In: *Boundary Layer and Flow Control*, edited by G. V. Lachmann, Vol. 1, Pergamon Press, Oxford, England, U.K., 1961, pp. 453–62.

[29] Coello, C. A., Lamont, G. B., and Van Veldhuizen, D. A., *Evolutionary Algorithms for Solving Multi-Objective Problems*, Springer–Verlag, New York, 2007.

[30] "MATLAB® Genetic Algorithm and Direct Search Toolbox™ 2: User's guide," The MathWorks, Inc., 2009.